Aligned Carbon Nanotube Morphogenesis Predicts Physical Properties of their Polymer Nanocomposites

Bharath Natarajan,[a,b#†] Itai Y. Stein,[c,d†] Noa Lachman,[c,e] Namiko Yamamoto,[c,f] Douglas S. Jacobs,[d] Renu Sharma,[a] J. Alexander Liddle,[a] Brian L.Wardle [c]*

[a]Center for Nanoscale Science and Technology, National Institute of Standards and Technology, Gaithersburg, Maryland 20899, USA.[b]Corporate Strategic Research, ExxonMobil Engineering and Research Company, Annandale, NJ, 08801, USA. [c]Department of Aeronautics and Astronautics, Massachusetts Institute of Technology, Cambridge, Massachusetts 02139, USA. [d]Department of Mechanical Engineering, Massachusetts Institute of Technology, Cambridge, Massachusetts 02139, USA [e]Department of Materials Science and Engineering, Tel Aviv University, Tel Aviv 6997801, Israel. [e]Department of Aerospace Engineering, The Pennsylvania State University, University Park, Pennsylvania 16802, USA.

† These authors contributed equally to this work

This work was primarily done while at the Center for Nanoscale Science and Technology, National Institute of Standards and Technology, Gaithersburg, Maryland 20899, USA

1. Tomography and Image Analysis

1.1. 3D Reconstruction/Volume Fraction

The morphological information from tomographic TEM referenced in the main text is provided in Figures S1, S2, and S3.

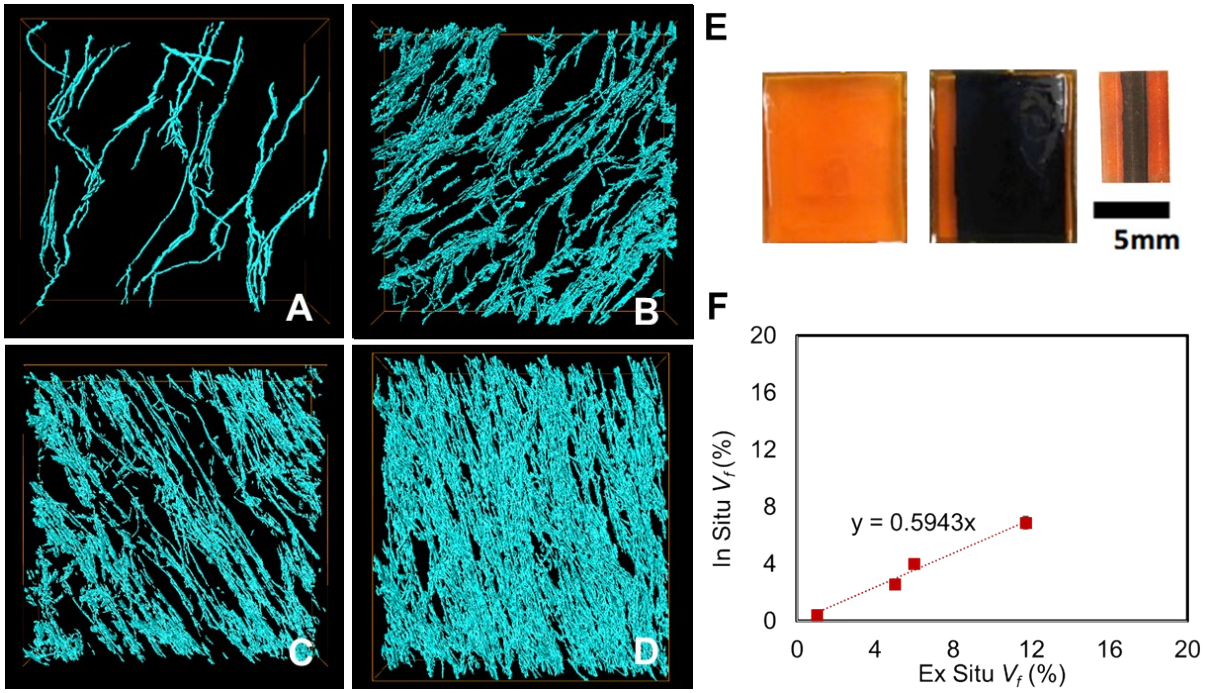

Figure S1. Volume-rendered reconstructions of (a) (0.44 ± 0.01) %, (b) (2.58 ± 0.25) %, (c) (4.04 ± 0.19) %, (d) (6.89 ± 0.43) % *in situ* V_f of A-CNT polymer nanocomposites (A-PNCs). The size of reconstructed volumes are: (a) 969 nm × 952 nm × 324 nm (b) 850 nm × 840 nm × 152 nm (c) 848 nm × 836 nm × 177 nm and (d) 764 nm × 841 nm × 211 nm.[1] (e) (L to R) Images of neat epoxy (orange color), (0.44 ± 0.01) % and (6.89 ± 0.43) *in situ* V_f A-PNCs (black color) embedded in epoxy (f) Plot of the *in-situ* V_f *versus* as-densified *ex situ* V_f for the four V_fs of aligned-CNT nanocomposites shown in (a)-(d). Dashed line represents a straight line fit to the data. The uncertainties, which represent one standard deviation in measurements of 3 samples per nanocomposite V_f, are not visible as the error bars are smaller than the datapoints.

1.2 CNT-CNT Proximity

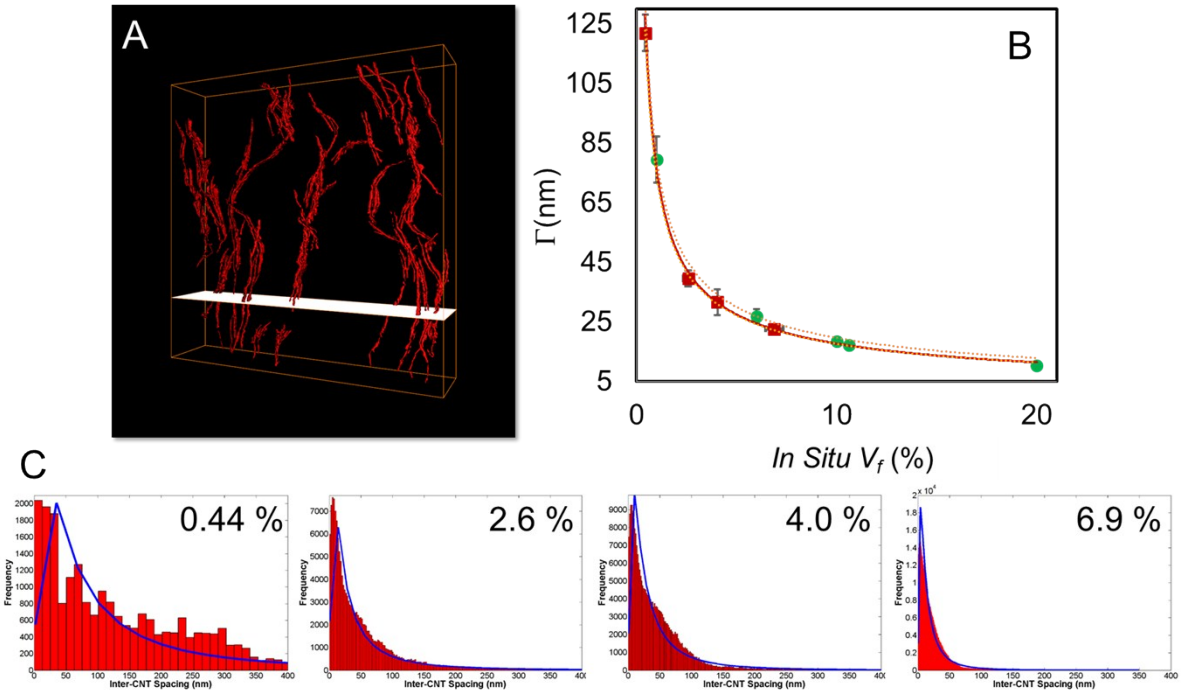

Figure S2. Average CNT-CNT spacing and junction distances from tomographic TEM data and reconstructions: (a) Volume rendered reconstruction of representative (0.44 ± 0.01) %V_f sample, with typical cross-sectional XZ slice indicated. The centroids of the CNT cross-sections from every XZ slice in the reconstructed volume are obtained by particle analysis on ImageJ and stored along with the slice number. The inter-centroid distances are then calculated using Delaunay triangulation.[1] The angle corrected average centroid distance minus the diameter of the CNTs is taken to be the average inter-CNT spacing (Γ) for the sample. (b) Average inter-CNT spacing (Γ, nm) calculated from tomographic reconstructions of aligned CNT composites (■, uncertainties represent one standard deviation in measurements of 3 samples per nanocomposite V_f) and from SEM images of densified forests (●, uncertainties as indicated by Stein et. al.[2,3]) *versus in situ* V_f. (c) Representative histograms (binned by Freedman-Diaconis rule) of inter-CNT spacing measured from volumes shown in Figure S1, fit with log-normal distributions.

1.3 Waviness

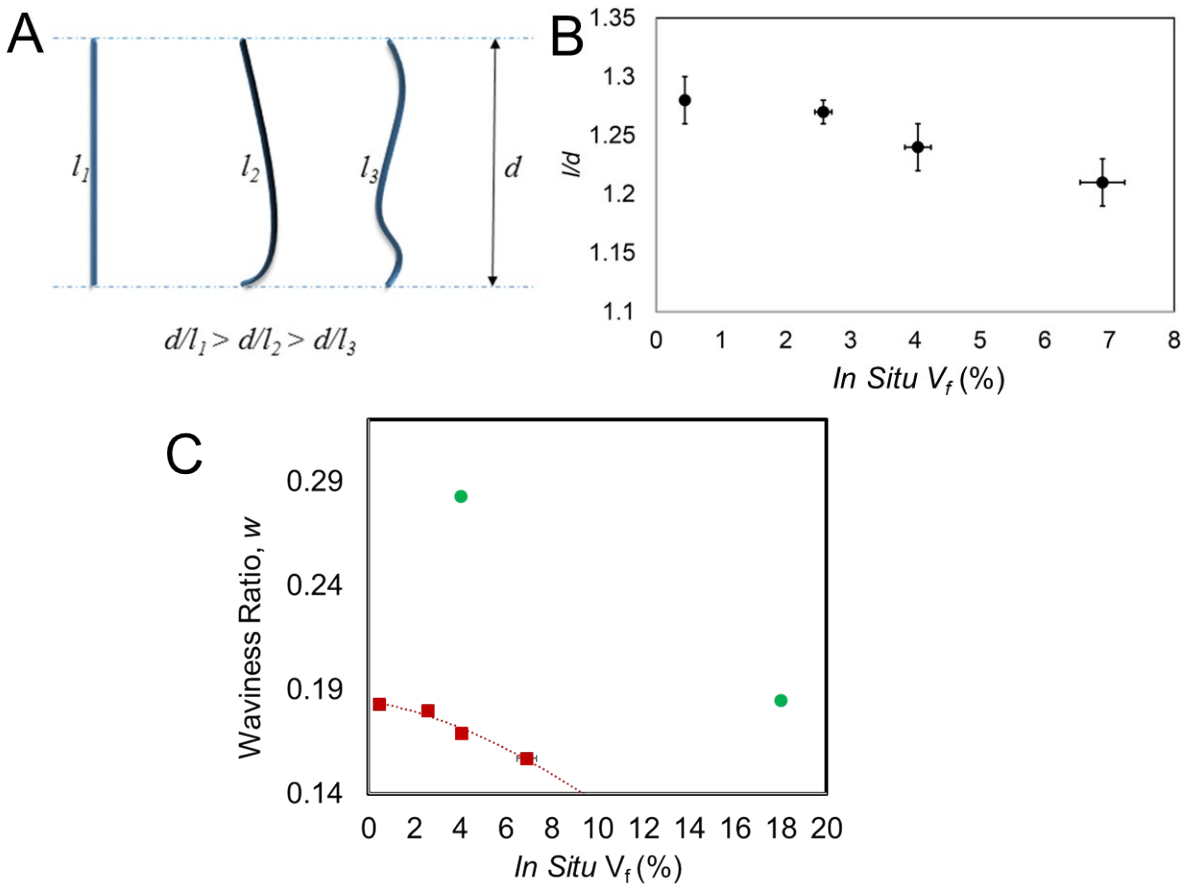

Figure S3. A-CNT tortuosity and waviness: (a) Illustration of CNTs with varying degrees of tortuosity (*l/d*) (b) Tortuosity plotted versus the *in situ* volume fraction (%). (d) 2D waviness ratio calculated from tomographic reconstruction of A-CNT composites (■, uncertainties represent one standard deviation in measurements of 3 samples per composite V_f) and SEM images of densified forests (●) *versus* the v_f.

The 2D CNT waviness in Figure S3d, defined as the ratio of the amplitude to the wavelength $(w = a/2\pi)$ of a sinusoidal function of the form $y = a\,cosx$ (where a is the amplitude) may be obtained from the tortuosity as below.

$$\frac{\pi}{\pi \int_{-\pi/2}^{\pi/2} \sqrt{1 + a^2 sin^2(x)}\, dx} = \frac{l}{d} \quad \text{(S1)}$$

Although the 2D waviness is in general agreement with those measured from SEM images of as-grown forests (w_{forest}) in prior work, we find the values measured from polymer infiltrated composites ($w_{composite}$) to be much lower (e.g., at 4 vol %, $w_{composite}$ = 0.169 and w_{forest} = 0.283; w_{forest} at 18 vol % ~ $w_{composite}$ at 0.44% ~ 0.185),[4] further highlighting the need for *in situ* assessments of the CNT morphology as done here even in a simple and well-controlled PNC fabrication process as used in processing the A-CNTs via RTM6 epoxy infiltration to A-PNCs. We surmise that stresses applied by the epoxy matrix during infiltration (capillary-assisted wetting, or wicking) and curing are responsible for this partial "ironing out" of the waviness. The trends in waviness (w) with V_f for the random helical system was found to follow the equation: $\Lambda(a_1(V_f)^{b_1} + c_1 \pm c_2)$, where a_1 = -0.04967, b_1 = 0.3646, c_1 = 0.2012, and c_2 = 0.008, and Λ was evaluated to be 0.68 ± 0.04. [5]

A-PNC modeling results are shown in Figures S4 and S5 to supplement the mechanical modeling discussion in the main text; similarly, Figure S7 for thermal and electrical conduction.

2. Properties

2.1 Mechanical Properties

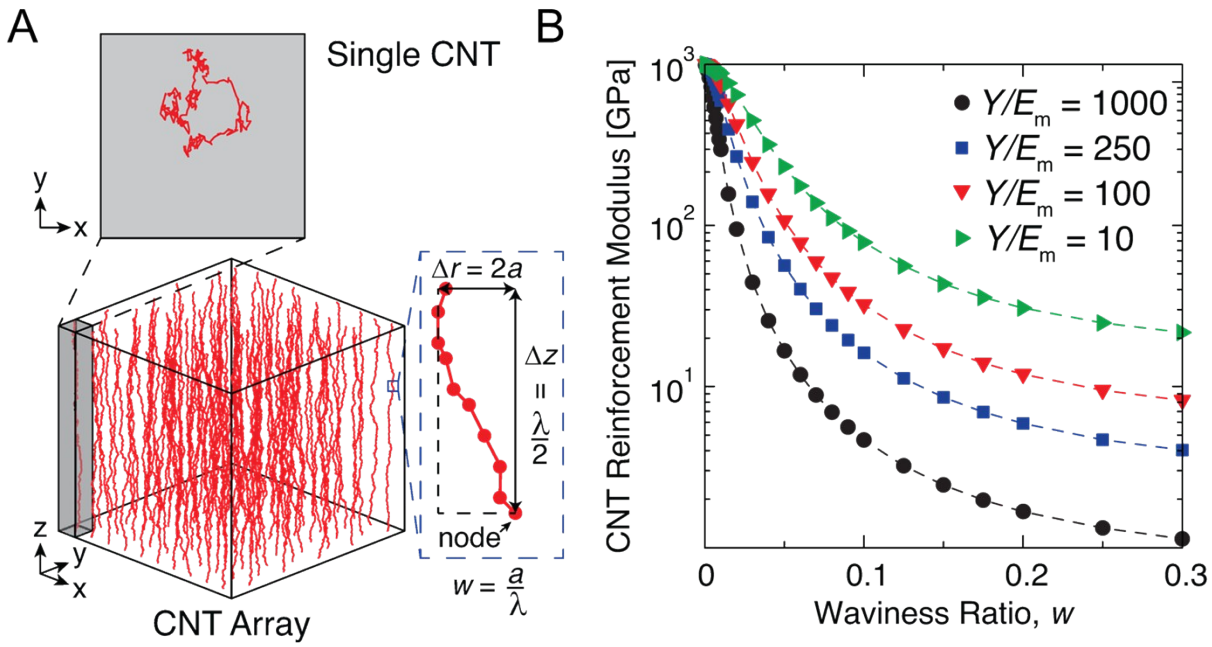

Figure S4. A-PNC random helical morphology and predicted CNT reinforcement modulus, after [5]: (a) Illustration showing top view of representative random helical CNT from a typical A-CNT ensemble employed in simulations (c) Plot of CNT reinforcement modulus (*Eo*) versus the waviness ratio (*w*) for various CNT modulus (*Y* = 1000 GPa) to matrix modulus (*Em*) ratios after [6].

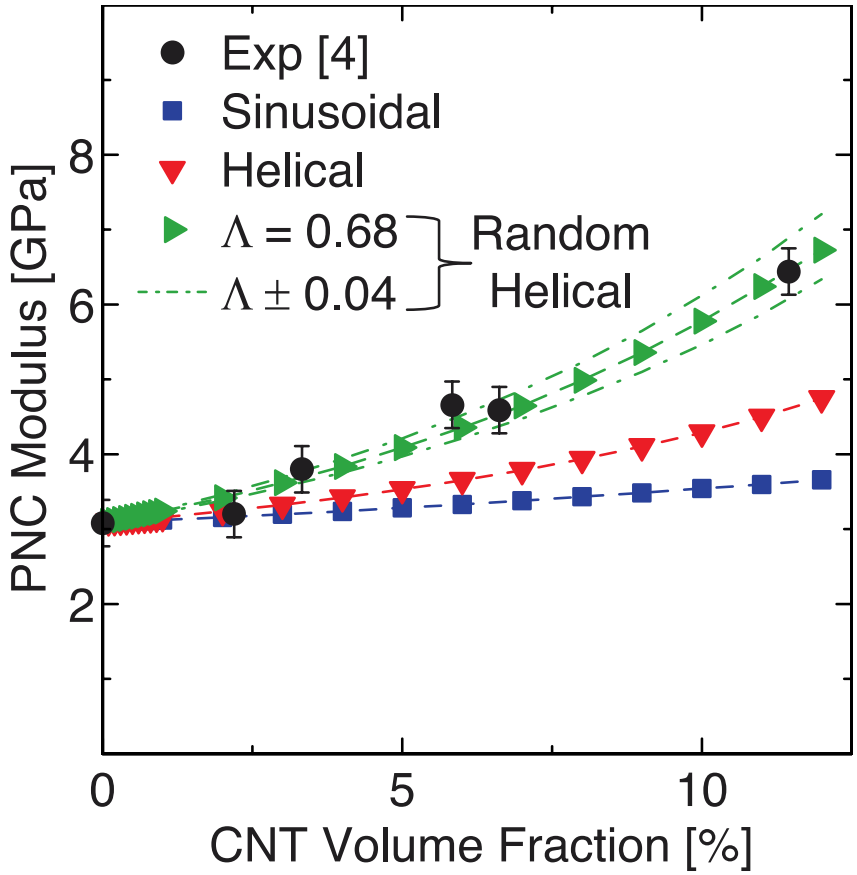

Figure S5. Plot of A-PNC modulus from Handlin et al.[4] versus *in situ* CNT V_f, with predictions from sinusoidal, helical and random helical waviness formulations shown. The under-prediction of properties by the sinusoidal and helical models is most likely because these idealized formulations overlook the stochastic mechanisms that lead to CNT waviness during growth and polymer infiltration. In reality there is significant nanoscopic surface roughness and CNT wall perturbation, which are only captured *via* the 'random' helical definition of the waviness.[7,8]

2.2 Transport Properties

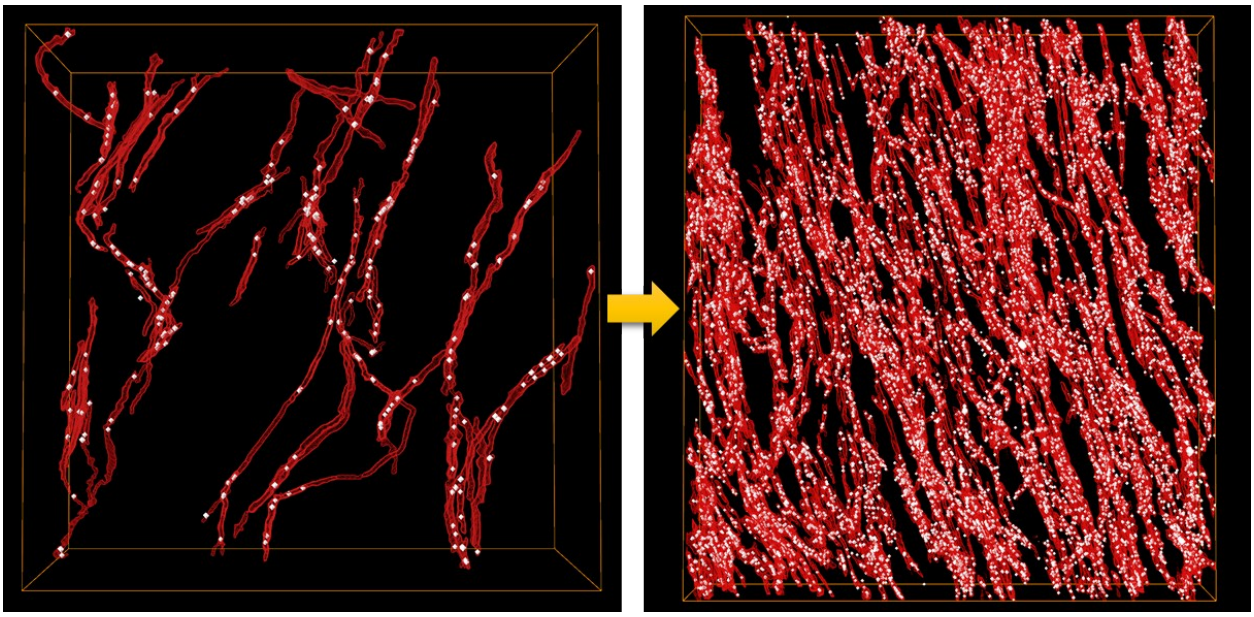

Figure S6. Volume-rendered reconstructions of (a) (0.44 ± 0.01) % and (b) (6.89 ± 0.43) *in situ* V_f of A-PNCs shown in Figure S1. The CNT-CNT junctions are highlighted by white dots to visualize the increase in junction density with V_f.

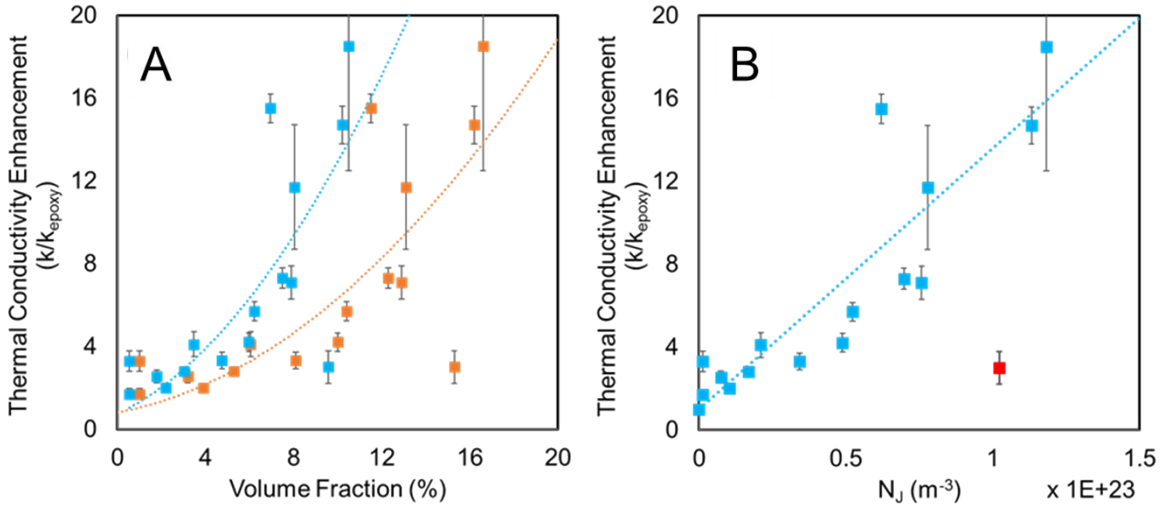

Figure S7. A-PNC axial thermal conductivity enhancements over neat epoxy, measured from the A-PNC samples studied in Marconnet *et al. versus*: (a) the originally reported using *ex situ* (■) and corrected or *in situ* (■) V_{ff}s (The dashed lines represent the power-law fits to the data) (b) the *estimated* CNT-CNT junction density (N_J, m^{-3}), showing linear scaling. Uncertainties indicated are standard deviations as measured by Marconnet et. al.[9]

2.3 Discussion on alternate sources of thermal conduction in A-PNCs:

We note that the dependence of thermal conductivity on CNT-CNT contact density discussed in the main text may only be true under certain conditions.[10,11] Computational studies suggest that the thermal boundary resistance (TBR) between a CNT and polymer has to be low (~ 10^{-8} to 10^{-9} m^2K/W), particularly in the transverse conduction orientation, compared to the resistance of the matrix.[10,12] Shenogina *et al*. find that at relatively high TBRs, the heat dissipation between tubes in contact and at separations up to 100 nm are identical due to thermal shielding by the matrix.[11] For similar reasons, Duong *et al.* observe the transverse thermal conductivity in A-CNT nanocomposites to be larger than the matrix only at low TBRs.[10] Since Marconnet *et al.* demonstrate a relatively small increase in the transverse conductivity in these systems, we deduce that the CNT-matrix TBRs are indeed relatively low here. While a low TBR is a necessary condition, it is not sufficient. The increasing trend in the thermal conductivity *versus* N_J plot also supposes that the CNT-CNT TBR is comparable to or smaller than the CNT-polymer TBR. Experimental work finds the area-normalized contact thermal resistance between aligned CNTs to be on the order of 10^{-9} m^2K/W at room temperature,[13] indicating that the necessary and sufficient conditions for the positive effect of CNT-CNT contacts are likely to have been met in the nanocomposites studied here comprised of multi-walled A-CNTs and an epoxy matrix. With the new morphological information presented here, future work to calculate the CNT-CNT and CNT-polymer TBRs is enabled. The 3D morphological data provides further insight into morphological features needed for such modeling.

Ensemble measurements on long CNT arrays have shown variations in the CNT alignment and network structure along the height of the array.[14] Furthermore, these studies note that CNTs may fail to traverse the entire thickness of the array,[14] (or to extend to the surface of the polymer) leading to poor engagement with the source and sink. Since these systems lack perfect alignment and likely continuity, the increased clustering with V_f also leads to an increased participation of "lost" CNTs in transport phenomena and therefore higher thermal conductivities. From 3D object counting,[15] we find that the volume fraction of the most prominent bundle increases relatively linearly with the V_f increase at first, but that the CNTs merge into large clusters (occupying > 40 % of the CNT volume) as the total V_f increases beyond 4 % (Figure S8a-d). Assuming that, at the theoretical packing limit of 83.45 %, the largest bundle volume fraction equals the total volume fraction,[2] we fit a 4 parameter asymmetric growth function through the plot of V_f of most prominent network *versus* the measured V_f ($y = 1.453(1 - 1/(1 + (\frac{x}{70.49})^{1.69}$) in Figure S8e. This fit captures the slow bundling of CNTs at low V_fs, the rapid increase in the rate of bundle formation beyond 4%, and the slowing of the same process when CNT spacings are smaller than or comparable to CNT diameters (Figure S8e, inset). We employ this function to estimate the V_fs of the most prominent network for the corrected volume fractions in Marconnet *et al.*'s data. Again, we observe a nearly linear trend in our plot of thermal conductivity enhancement *versus* the V_f of the most prominent network, suggesting that the non-linear increase in the engagement of CNTs in conduction leads in part to the non-linearity in the measured thermal property data (**Figure 4f**). We note that this parameter might implicitly account for the effects of CNT contacts.

Another potentially influential factor causing the non-linearity is the improvement in the alignment quality of the CNT arrays with densification. The increase in CNT alignment has been theoretically and experimentally found to decrease CNT-CNT contact resistance due to the increase in contact area going from a cross contact to an aligned contact: CNTs crossing at 90̊ were determined to have 2 orders of magnitude larger resistance than parallel CNTs in contact.[13,16] The new TEM 3D reconstructions allow us to determine the structure tensors of the individual CNTs, and quantify the distribution around the CNT's mean alignment (regardless of the specimen alignment, Figure S9a-d**)**.[17] From this data, we find that the degree of alignment improves with increasing V_f due to the increased spatial restriction imposed by bundling/clustering. This improvement is shown in the plot of angular dispersion (one standard deviation in the distribution of orientations about the mean) *versus in situ* V_f (Figure S9e). We observe a steady decrease in dispersion of orientations with increasing V_f, suggesting that a higher percentage of contacts are between CNTs crossing at low angles, which could lead to improved transport through CNT junctions. While in the lateral direction this improved alignment is not of particular importance,[12] along the CNT axis the CNT resistance could drop significantly, thereby explaining why anisotropy increases with V_f.

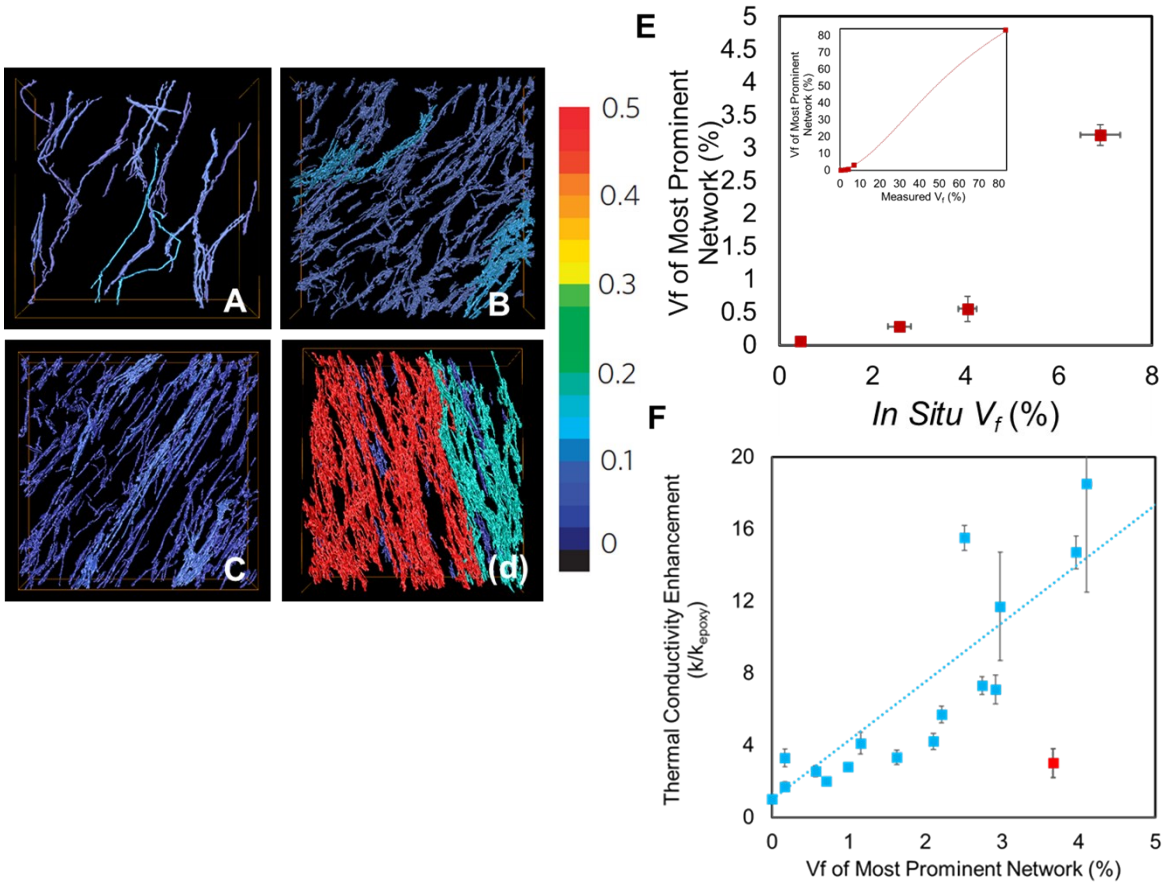

Figure S8. Analysis of bundling and other morphological descriptors contributing to non-linear thermal conductivity increase with *in situ* V_f of A-CNTs in A-PCNs: Connectivity-analyzed 3D visualizations of (a) 0.44 % (b) 2.6 % (c) 4 % and (d) 6.9 % *in situ* V_f of A-PNCs obtained from sample volumes shown in Figure 1, with individual clusters labeled according to the adjacent color scale. The units on the scale represent the fraction of CNT *in situ* V_f occupied by individual bundles. As is evident, at loadings above 4 % the CNTs cluster into larger bundles. (e) the volume fraction of the most prominent network *versus* the *in situ* V_f for the four V_fs of aligned-CNT nanocomposites studied here. The inset shows the fit through the data with limits at 83.45 %. The uncertainties represent one standard deviation in measurements of 3 samples per composite V_f. and (c) the volume fraction of the most prominent network. (f) A-PNC axial thermal conductivity enhancements over neat epoxy, measured from the A-PNC samples studied in Marconnet *et al. versus* the estimated V_f of the most prominent bundle.

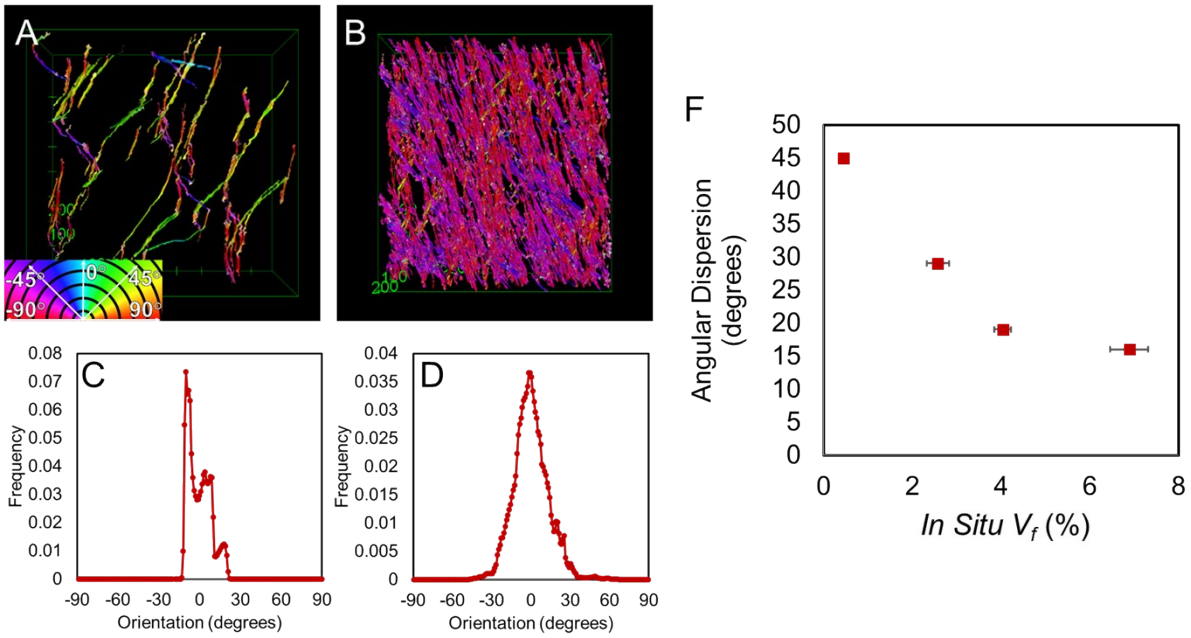

Figure S9. Color-coded orientation analysis of (a) 0.44 % and (b) 6.9% CNT, respectively. (c) and (d) – plotted frequency *versus* orientation of the volumes in (a) and (b), respectively. (f) Angular Dispersion (°) *versus* the *in situ* V_f. The uncertainties represent one standard deviation in measurements of 3 samples per composite V_f.

1 B. Natarajan, N. Lachman, T. Lam, D. Jacobs, C. Long, M. Zhao, B. L. Wardle, R. Sharma and J. A. Liddle, *ACS Nano*, 2015, **9**, 6050–6058.

2 I. Y. Stein and B. L. Wardle, *Phys. Chem. Chem. Phys.*, 2013, **15**, 4033.

3 H. Cebeci, I. Y. Stein and B. L. Wardle, *Appl. Phys. Lett.*, 2014, **104**, 023117.

4 D. Handlin, I. Y. Stein, R. G. de Villoria, H. Cebeci, E. M. Parsons, S. Socrate, S. Scotti and B. L. Wardle, *J. Appl. Phys.*, 2013, **114**, 224310.

5 I. Y. Stein and B. L. Wardle, *Nanotechnology*, 2016, **27**, 035701.

6 I. Y. Stein, D. J. Lewis and B. L. Wardle, *Nanoscale*, 2015, **7**, 19426–19431.

7 V. Balakrishnan, M. Bedewy, E. R. Meshot, S. W. Pattinson, E. S. Polsen, F. Laye, D. N. Zakharov, E. A. Stach and A. J. Hart, *ACS Nano*, 2016, **10**, 11496–11504.

8 E. R. Meshot, D. W. Zwissler, N. Bui, T. R. Kuykendall, C. Wang, A. Hexemer, K. J. J. Wu and F. Fornasiero, *ACS Nano*, 2017, **11**, 5405–5416.

9 A. M. Marconnet, N. Yamamoto, M. A. Panzer, B. L. Wardle and K. E. Goodson, *ACS Nano*,

2011, **5**, 4818–4825.

10 H. M. Duong, N. Yamamoto, K. Bui, D. V. Papavassiliou, S. Maruyama and B. L. Wardle, *J. Phys. Chem. C*, 2010, **114**, 8851–8860.

11 N. Shenogina, S. Shenogin, L. Xue and P. Keblinski, *Appl. Phys. Lett.*, 2005, **87**, 133106.

12 H. M. Duong, N. Yamamoto, D. V Papavassiliou, S. Maruyama and B. L. Wardle, *Nanotechnology*, 2009, **20**, 155702.

13 J. Yang, S. Waltermire, Y. Chen, A. A. Zinn, T. T. Xu and D. Li, *Appl. Phys. Lett.*, 2010, **96**, 023109.

14 M. Bedewy, E. R. Meshot, M. J. Reinker and A. J. Hart, *ACS Nano*, 2011, **5**, 8974–8989.

15 M. Doube, M. M. Kłosowski, I. Arganda-Carreras, F. P. Cordelières, R. P. Dougherty, J. S. Jackson, B. Schmid, J. R. Hutchinson and S. J. Shefelbine, *Bone*, 2010, **47**, 1076–1079.

16 A. M. Marconnet, M. A. Panzer and K. E. Goodson, *Rev. Mod. Phys.*, 2013, **85**, 1295–1326.

17 R. Rezakhaniha, A. Agianniotis, J. T. C. Schrauwen, A. Griffa, D. Sage, C. V. C. Bouten, F. N. Van de Vosse, M. Unser and N. Stergiopulos, *Biomech. Model. Mechanobiol.*, 2012, **11**, 461–473.